

# Water Contributes to Higher Energy Density and Cycling Stability of Prussian Blue Analogue Cathodes for Aqueous Sodium-Ion Batteries

Xingyu Guo,<sup>†</sup> Zhenbin Wang,<sup>‡</sup> Zhi Deng,<sup>‡</sup> Xiangguo Li,<sup>‡</sup> Bo Wang,<sup>§</sup> Xi Chen,<sup>§</sup> and Shyue Ping Ong<sup>‡,\*</sup>

<sup>†</sup>Materials Science and Engineering Program, University of California San Diego, 9500 Gilman Dr, Mail Code 0418, La Jolla, California 92093-0448, United States

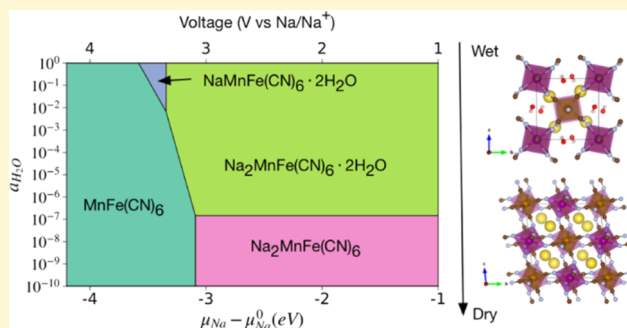
<sup>‡</sup>Department of NanoEngineering, University of California San Diego, 9500 Gilman Dr, Mail Code 0448, La Jolla, California 92093-0448, United States

<sup>§</sup>GEIRI North America, 250 West Tasman Drive, Suite 100, San Jose, California 95134, United States

## Supporting Information

**ABSTRACT:** In this work, we performed a comprehensive study of Prussian blue and its analogues (PBAs), one of the most promising cathode materials for aqueous sodium-ion batteries for large-scale energy-storage systems, using first-principles calculations. It is confirmed that dry PBAs generally undergo a phase transition from a rhombohedral  $\text{Na}_2\text{PR}(\text{CN})_6$  (where P and R are transition metals) to a tetragonal/cubic  $\text{PR}(\text{CN})_6$  during Na extraction, in agreement with experimental observations. Using a grand potential phase diagram construction, we show that water and Na co-intercalation result in fundamentally different phase transition behavior and, hence, electrochemical voltage profiles in wet versus dry electrolytes.

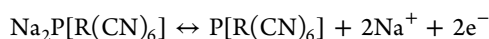
Lattice water increases the average voltage and reduces the volume change during electrochemical cycling, resulting in both higher energy density and better cycling stability. Finally, we identified four new PBA compositions,  $\text{Na}_2\text{CoMn}(\text{CN})_6$ ,  $\text{Na}_2\text{NiMn}(\text{CN})_6$ ,  $\text{Na}_2\text{CuMn}(\text{CN})_6$ , and  $\text{Na}_2\text{ZnMn}(\text{CN})_6$ , that show great promise as cathodes for aqueous rechargeable Na-ion batteries.



## INTRODUCTION

Aqueous sodium-ion batteries (ASIBs) are promising candidates for large-scale electric energy-storage applications due to their high rate capabilities, good cycling stabilities, and high safety.<sup>1</sup> Compared to conventional organic solvent electrolytes, aqueous electrolytes have a narrower stable voltage window of 1.23 V, beyond which the electrolysis of  $\text{H}_2\text{O}$  occurs. Consequently, one of the key challenges in ASIBs is the discovery of electrodes with suitable working potential and high moisture stability in aqueous electrolytes.

Recently, extensive efforts have been devoted to exploring new cathodes in ASIBs. Among them, Prussian blue and its analogues (PBAs) have been investigated intensively due to their excellent electrochemical properties. The chemical composition of PBAs can be expressed as  $\text{A}_x\text{P}[\text{R}(\text{CN})_6]_{1-y}\square_y \cdot n\text{H}_2\text{O}$ , where A is an alkali or alkaline metal ion, P and R are transition-metal ions, and  $\square$  indicates a  $\text{R}(\text{CN})_6$  vacancy. Both P and R can undergo reversible redox reactions



Various crystal structures of PBAs have been reported in the literature (Figure 1). Prussian blue ( $\text{Fe}_4[\text{Fe}(\text{CN})_6]_3 \cdot x\text{H}_2\text{O}$ ) crystallizes in a face-centered cubic phase (spacegroup:

$\text{Fm}\bar{3}m$ ).<sup>2</sup> Under Na-deficient conditions, some PBAs form a tetragonal lattice due to the elongation of  $c$ -axis caused by Jahn–Teller effects of certain transition metals, such as  $\text{Mn}^{3+}$ .<sup>3,4</sup> When different amounts of Na ions and water molecules enter the PBAs lattice, the symmetry of the crystal is further reduced to form monoclinic and rhombohedral structures.<sup>3–6</sup> Figure 1a shows the cubic/tetragonal PBA crystal structure, in which the transition metals are 6-fold coordinated by nitrogen and carbon atoms connected through cyanide (CN) ligands. In the monoclinic (Figure 1b) and rhombohedral (Figure 1c) phases, the octahedra twist and Na ions are displaced from the face-centered sites. The open three-dimensional (3D) framework of PBAs enables fast ionic diffusion as well as stable cycling stability during alkali intercalation/deintercalation.

There have been extensive experimental studies of PBA-based cathodes in both aqueous and nonaqueous SIBs. To optimize the performance of PBA-based electrodes in SIBs, one common practice is to substitute the P and R sites with

Received: June 10, 2019

Revised: July 15, 2019

Published: July 18, 2019

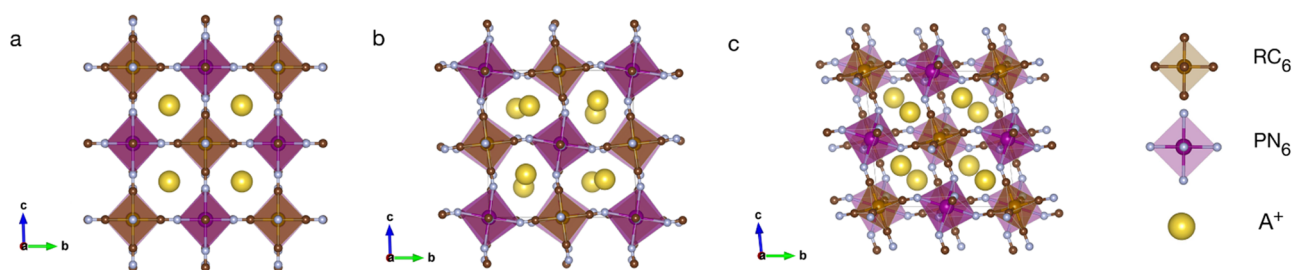


**Figure 1.** Crystal structures of PBAs. (a) Cubic/tetragonal (spacegroup:  $Fm\bar{3}m$  or  $I4/mmm$ ), (b) monoclinic (spacegroup:  $P2_1/c$ ), and (c) rhombohedral (spacegroup:  $R\bar{3}$ )

different transition metals. For example, in organic electrolytes, the  $\text{Na}_x\text{FeFe}(\text{CN})_6$  compound has been reported to exhibit a reversible  $\text{Na}^+$  insertion capacity of  $120 \text{ mAh g}^{-1}$  with 87% capacity retention over 500 cycles.<sup>7</sup> By replacing the P site with Ni, the reversibility can be further improved by limiting the amount of Na intercalated to 1 and, hence, the volume change with cycling, and a zero capacity loss after 5000 cycles has been observed in the aqueous electrolyte.<sup>8</sup> When both the P and R sites are replaced by Mn, an exceptionally high capacity of  $>200 \text{ mAh g}^{-1}$  has been achieved ( $\text{Mn}^{3+}\text{Mn}^{3+} \rightarrow \text{Mn}^{2+}\text{Mn}^+$ ).<sup>9</sup> Due to the flexibility of the PBA structure, there remains a wide unexplored space of PBAs.

Depending on experimental conditions, various phase transitions and polymorphs of PBAs along with distinct electrochemical behaviors have been reported. Also, the existence of lattice water in PBAs further complicates their structural and electrochemical properties. For example, Song et al. have reported that the existence of coordinating water molecules in  $\text{Na}_2\text{MnFe}(\text{CN})_6$  cathodes not only affects its crystal structure but also changes the shape of its voltage profile in a 1:1 diethyl carbonate (DEC)/ethylene carbonate (EC) electrolyte.<sup>3</sup> Although lattice water is generally believed to have a detrimental effect on the transport of  $\text{Na}^+$  ions,<sup>10</sup>  $\text{KCuFe}(\text{CN})_6$  and  $\text{Na}_2\text{NiFe}(\text{CN})_6$  have been shown to have better cycling stability in aqueous electrolytes than those in organic electrolytes.<sup>8,11</sup> The hydrated low-defect  $\text{Na}_2\text{MnFe}(\text{CN})_6$  has been determined to crystallize in the monoclinic phase along with two coordination  $\text{H}_2\text{O}$  per formula by X-ray diffraction (XRD) techniques.<sup>3</sup> The O atoms have been shown to occupy the large interstitial sites and form zig-zag Na–O chains interpenetrating the 3D framework. Similar results have been reported for hydrated  $\text{Na}_2\text{MnMn}(\text{CN})_6$ . The structure of  $\text{Fe}_4[\text{Fe}(\text{CN})_6]_3 \cdot 14\text{H}_2\text{O}$  has also been investigated by the neutron diffraction experiment.<sup>2</sup> Due to the randomly distributed  $\text{Fe}(\text{CN})_6$  vacancies, the  $\text{Fe}_4[\text{Fe}(\text{CN})_6]_3 \cdot 14\text{H}_2\text{O}$  crystal deviates from the face-centered cubic symmetry, and the water molecules occupy both the empty N sites of  $\text{Fe}(\text{CN})_6$  vacancies and the interstitial positions. Therefore, understanding how the presence of water influences the phase evolution with alkali intercalation may help to enhance the performance of PBA cathodes as well as contribute to their development in ASIBs.

Although density functional theory (DFT) calculations have been extensively used in the study and design of alkali-ion battery cathodes,<sup>12–16</sup> there have only been a few attempts to use DFT calculations to provide insights into PBA cathodes, probably due to the complexity of the PBA phase space and the complicating effects of the lattice water. Ling et al. have shown that the intercalation of different cations into  $\text{FeFe}(\text{CN})_6$  cathodes in organic electrolytes is strongly affected by the

ionic radius.<sup>17</sup> Xiao et al. have also studied the structural evolution of both dry and hydrated  $\text{Na}_2\text{MnFe}(\text{CN})_6$  cathodes upon Na intercalation and found that during Na intercalation, the dehydrated material undergoes a direct phase transition from the orthorhombic to rhombohedral phase, whereas the hydrated one stays in the monoclinic phase and shows a stable phase at an intermediate Na concentration.<sup>18</sup> However, their model for the hydrated phase was simplified to reproduce the correct voltage profile observed in the experiment.

In this work, we performed a comprehensive study of the phase evolution of PBA cathodes in the presence of water as well as with Na intercalation. Under dry conditions, it is found that the most stable Na-rich PBA structure is always the rhombohedral phase, whereas the most stable Na-deficient structure is either the cubic or tetragonal phase. Using DFT grand potential phase diagrams, we show that water and Na co-intercalation behavior under different electrolyte conditions causes distinct phase transition phenomena during electrochemical reaction processes and generally increases the Na insertion voltage. Using these insights, we identified four promising aqueous Na-ion cathodes in the PBA structure using a broad suite of descriptors.

## THEORETICAL APPROACH

**Computational Details.** All density functional theory (DFT) calculations were performed using the Vienna Ab initio simulation package within the projected-augmented wave method.<sup>19,20</sup> The screened hybrid Heyd–Scuseria–Ernzerhof (HSE) functional<sup>21</sup> was used to obtain an accurate structural description and energies of PBAs. All analyses were carried out using HSE-computed quantities, unless otherwise stated. We have also benchmarked the Perdew–Burke–Ernzerhof (PBE) generalized gradient approximation (GGA)<sup>22</sup> and PBEsol functionals with the Hubbard U extension (PBE + U)<sup>23</sup> as well as the strongly constrained and appropriately normed (SCAN) meta-GGA with van der Waals (vdW) functional implemented (SCAN + rrv10)<sup>24</sup> in terms of their ability to predict the average voltage of PBAs cathodes. For all structural optimizations and total energy calculations, energies and forces were converged to within  $10^{-5} \text{ eV}$  and  $0.05 \text{ eV \AA}^{-1}$ , respectively, and a k-point density of at least  $1000/(\text{number of atoms in the unit cell})$  and an energy cutoff of 520 eV were used. All  $\text{Na}_2\text{PR}(\text{CN})_6$  were initialized with P and R in the 2+ oxidation state, whereas different initializations of oxidation states ( $\text{P}^{3+}\text{R}^{3+}$ ,  $\text{P}^{4+}\text{R}^{2+}$ ,  $\text{P}^{2+}\text{R}^{4+}$ ) for  $\text{PR}(\text{CN})_6$  were evaluated to identify the lowest-energy configuration. PBAs have been shown to exhibit various spin-ordering configurations with temperatures, compositions, and photoinduction.<sup>25–27</sup> For all polymorphs, we calculated the total energies of all possible spin-ordering configurations, and the lowest-energy one was

used for the property calculations (Table S1). In this work, only ferromagnetic configurations were considered based on previous results from Nishino et al.<sup>27</sup> All crystal structure manipulations and data analyses were performed using the Python Materials Genomics (pymatgen) package.<sup>28</sup>

**Average Voltage.** The average intercalation voltage vs Na/Na<sup>+</sup> was calculated based on the following formula<sup>29</sup>

$$V = \frac{E(\text{Na}_x\text{P}[\text{R}(\text{CN})]_6) - E(\text{Na}_{n-x}\text{P}[\text{R}(\text{CN})]_6) - xE(\text{Na})}{xe}$$

**Grand Potential Diagram.** Grand potential phase diagrams have been used to study open electrochemical systems.<sup>30,31</sup> For the Na<sub>x</sub>P[R(CN)<sub>6</sub>] system open to H<sub>2</sub>O and Na, the relevant thermodynamic potential is the grand potential ( $\Phi$ ), defined as

$$\Phi = G_{\text{Na}_x\text{P}[\text{R}(\text{CN})]_6 \cdot n_{\text{H}_2\text{O}}} - n_{\text{H}_2\text{O}}\mu_{\text{H}_2\text{O}} - n_{\text{Na}}\mu_{\text{Na}}$$

where  $G_{\text{Na}_x\text{MnFe}(\text{CN})_6 \cdot n_{\text{H}_2\text{O}}}$  is the Gibbs free energy, which can be approximated by the computed HSE energy at 0 K for solids,<sup>30</sup>  $n_{\text{H}_2\text{O}}$  and  $\mu_{\text{H}_2\text{O}}$  are the number of H<sub>2</sub>O molecules per formula and the chemical potential of H<sub>2</sub>O, respectively, and  $n_{\text{Na}}$  and  $\mu_{\text{Na}}$  are the number and chemical potential of Na, respectively.

The chemical potential of liquid H<sub>2</sub>O can be expressed as

$$\mu_{\text{H}_2\text{O}(\text{l})}^0 = \mu_{\text{H}_2\text{O}(\text{l})}^0 + RT \ln a_{\text{H}_2\text{O}(\text{l})}$$

where  $\mu_{\text{H}_2\text{O}(\text{l})}^0$ ,  $a_{\text{H}_2\text{O}(\text{l})}$ ,  $R$ , and  $T$  are defined as the chemical potential of liquid H<sub>2</sub>O in its standard state, the activity of H<sub>2</sub>O in the electrolyte, the universal gas constant, and temperature, respectively. By assigning various values to  $a_{\text{H}_2\text{O}(\text{l})}$ , different electrolyte conditions can be simulated.

Previously, Gautam et al. have derived the reference chemical potential for liquid H<sub>2</sub>O from the PBE-computed energy of H<sub>2</sub>O vapor and the enthalpy of evaporation, which has been shown to reproduce the oxide- > hydroxide formation energies of main-group metals.<sup>31</sup> Using a similar approach with HSE-computed energies, we obtained  $\mu_{\text{H}_2\text{O}(\text{l})}^0 = -19.566$  eV. Separately, Nørskov et al. have computed the reference chemical potential for liquid H<sub>2</sub>O by calculating the total energy of H<sub>2</sub>O vapor at 0.035 bar as the reference state because at this pressure, gas-phase H<sub>2</sub>O is in equilibrium with liquid water at 300 K.<sup>32</sup> Using this approach with HSE-computed energies, we obtained  $\mu_{\text{H}_2\text{O}(\text{l})}^0 = -18.866$  eV. In this work, we derived a  $\mu_{\text{H}_2\text{O}(\text{l})}^0$  for PBA compounds by considering the following neutralization reaction of hydrogen cyanide and alkali hydroxide



where A is an alkali metal. The enthalpy of liquid H<sub>2</sub>O can, therefore, be obtained by fitting the DFT-calculated energies of HCN vapor, solid AOH, and solid ACN with the experimental standard enthalpy of the reaction ( $\Delta H_r^{\text{exp}}$ ) obtained from the NIST Chemistry WebBook.<sup>33</sup> Due to limited experimental data, we performed this fitting using only two alkali metals Na and K. The DFT total energy of HCN was obtained by calculating the energy of a single molecule of HCN in a  $15 \times 15 \times 15 \text{ \AA}^3$  box, whereas the zero-point energy of HCN vapor was obtained from the calculated frequencies. The initial structures of AOH and ACN solids were obtained from the

Inorganic Crystal Structure Database<sup>34</sup> and then fully relaxed to obtain accurate total energy from DFT calculations. The chemical potential of pure liquid H<sub>2</sub>O is then obtained by the following formula

$$\mu_{\text{H}_2\text{O}(\text{l})}^0 = \Delta H_r^{\text{exp}} - (E_{\text{HCN}(\text{g})} + E_{\text{ZPE}(\text{HCN}(\text{g}))} + E_{\text{AOH}(\text{s})} + E_{\text{ACN}(\text{s})}) - TS_{\text{water}}$$

Using this approach, we derived a reference value of  $\mu_{\text{H}_2\text{O}(\text{l})}^0 = -19.165$  eV, which is in between the two reference values derived using the previous two approaches. We will discuss the implications of the reference  $\mu_{\text{H}_2\text{O}(\text{l})}^0$  in the Discussion section.

Finally, the chemical potential of Na,  $\mu_{\text{Na}}$ , is related to the voltage  $V$  with respect to the Na metal anode by

$$V = -\frac{\mu_{\text{Na}} - \mu_{\text{Na}}^0}{e}$$

where  $\mu_{\text{Na}}^0$  is the chemical potential of Na metal and  $e$  is the electron charge.

## RESULTS AND DISCUSSION

In this section, we will first present detailed benchmarks on five experimentally known PBA compositions, Na<sub>x</sub>PR(CN)<sub>6</sub> where (P, R) = (Mn, Mn), (Mn, Fe), (Fe, Fe), (Co, Fe), (Ni, Fe), followed by a comprehensive screening for new PBA compositions.

### BENCHMARKING OF EXCHANGE-CORRELATION FUNCTIONALS

The mixed-valence nature of PBAs leads to a rich electronic structure, which complicates the description of their properties by DFT calculations. Previous studies have showed that HSE functional is able to describe the structural and electronic properties of FeFe(CN)<sub>6</sub><sup>35</sup> as well as the sodium intercalation voltages of Na<sub>2</sub>MnFe(CN)<sub>6</sub>.<sup>18</sup> GGA + U methods have been shown to reach a good agreement with HSE functional only if different effective U values are applied to each site of FeFe(CN)<sub>6</sub>,<sup>35</sup> which hinders its application as a predictive tool in PBAs compounds. In the Materials Project, a set of U values for the various transition metals have been calibrated for transition-metal oxide systems.<sup>36,37</sup> We have also evaluated the performance of various exchange-correlation functionals (PBE,<sup>22</sup> PBE + U,<sup>37</sup> PBEsol,<sup>38</sup> PBEsol + U,<sup>37</sup> HSE,<sup>21</sup> SCAN,<sup>39</sup> SCAN + rVV10<sup>24</sup>) in reproducing experimental spin configuration, lattice parameters, and redox potentials of PBAs. From Table S2, it can be observed that only HSE, PBE + U, and PBEsol + U reproduce the experimental ground spin states for all tested Na concentrations. Furthermore, the HSE functional yields the most accurate lattice parameters with an error less than ~0.8% across all Na concentrations and for both wet and dry PBAs (Figure S1) as well as the most accurate voltages (Table S3).

Table 1 compares the voltages of five well-known PBAs computed using various exchange-correlation functionals with the experimentally measured voltages. We find that both the PBE + U and PBEsol + U functionals utilizing Materials Project-calibrated U values are not able to achieve even qualitative accuracy in predicting the voltage steps of Na<sub>2</sub>MnMn(CN)<sub>6</sub> and Na<sub>2</sub>FeFe(CN)<sub>6</sub>. In particular, NaMnMn(CN)<sub>6</sub> is not a stable intermediate in PBEsol + U, and NaFeFe(CN)<sub>6</sub> is not a stable intermediate in both PBE +

**Table 1. Calculated and Experimental Average Voltages for Five PBA Cathodes<sup>a</sup>**

formula	voltage (V vs Na/Na <sup>+</sup> )			
	exp.	PBE + <i>U</i>	PBEsol + <i>U</i>	HSE
Na <sub>2</sub> MnMn(CN) <sub>6</sub>	2.65/3.55 <sup>9</sup>	1.14/3.17	0.51	2.18/2.70
Na <sub>2</sub> MnFe(CN) <sub>6</sub>	3.53 <sup>3</sup>	3.17	3.18	3.10
Na <sub>2</sub> FeFe(CN) <sub>6</sub>	3.00/3.29 <sup>5</sup>	2.70	6.47	2.91/3.02
Na <sub>2</sub> CoFe(CN) <sub>6</sub>	3.12/3.42 <sup>6</sup>	2.63/3.55	2.73/3.65	3.04/3.06
Na <sub>2</sub> NiFe(CN) <sub>6</sub>	3.38 <sup>40</sup>	2.75	3.02	3.22

<sup>a</sup>Individual voltage step for Na<sub>2</sub>PR(CN)<sub>6</sub> → NaPR(CN)<sub>6</sub> and NaPR(CN)<sub>6</sub> → PR(CN)<sub>6</sub> are indicated if NaPR(CN)<sub>6</sub> is a stable intermediate in the computed pseudo-binary PR(CN)<sub>6</sub>-Na<sub>2</sub>PR(CN)<sub>6</sub> 0 K stability diagram for the functional

*U* and PBEsol + *U*. Furthermore, the voltages from the HSE functional are in much better agreement with the experimental voltages compared to those of PBE + *U* and PBEsol + *U*. Except for Na<sub>2</sub>MnMn(CN)<sub>6</sub>, the errors of all of the voltages calculated by HSE are within 0.5 V.

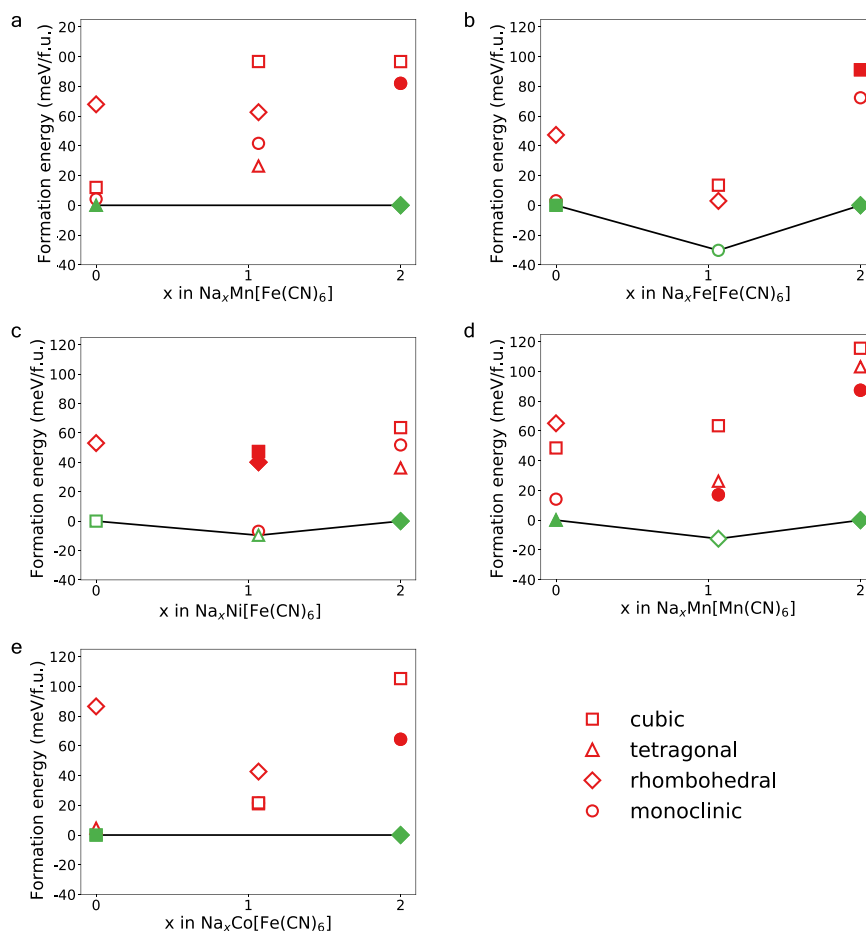
### ■ THERMODYNAMIC STABILITY AND NA INTERCALATION IN DRY PBAS

Figure 2 shows the calculated pseudo-binary stability diagrams for the five experimentally known PBAs at  $x_{\text{Na}} = 0, 1, 2$ . At full sodiation ( $x_{\text{Na}} = 2$ ), the most stable structure for all five PBAs is the densely packed rhombohedral phase (shown in Figure

1c). In all instances, the rhombohedral phase is more stable than the more open tetragonal, monoclinic, and cubic phases by more than 30 meV/atom. At full desodiation ( $x_{\text{Na}} = 0$ ), the less densely packed cubic and tetragonal phases (shown in Figure 1a,b, respectively) become more stable. The elongation of *c* axes in Na<sub>2</sub>MnFe(CN)<sub>6</sub> and Na<sub>2</sub>MnMn(CN)<sub>6</sub> to form the tetragonal phase is due to the Jahn–Teller effect of Mn<sup>3+</sup>.

Consequently, under equilibrium electrochemical processes, there is a reversible phase transition from the rhombohedral to cubic/tetragonal phase in dry PBA-based cathodes. This trend has been observed in experiments for many PBA compounds.<sup>3,5,6,40</sup> The phase transformations can be interpreted by the competition between the Coulombic interaction of Na<sup>+</sup> and N<sup>δ-</sup> atoms and the tendency to maximize *d*- $\pi$  orbital overlap.<sup>18</sup> The former effect tends to bend the bonds and tilt the polyhedral, whereas the latter straightens the lattice.

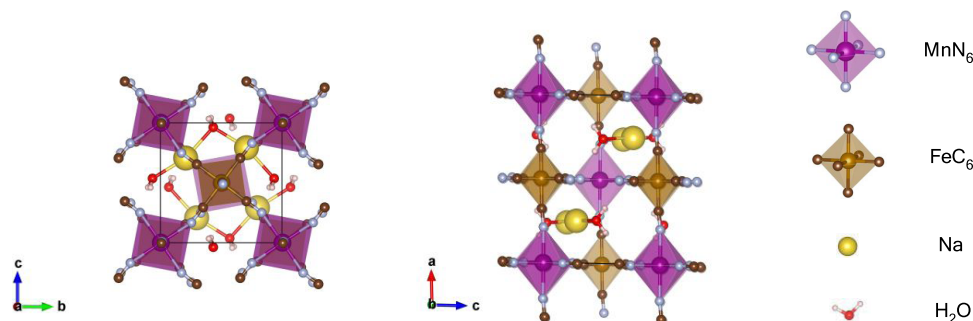
At  $x_{\text{Na}} = 1$ , only NaFeFe(CN)<sub>6</sub>, NaMnMn(CN)<sub>6</sub>, and NaNiFe(CN)<sub>6</sub> are predicted to be stable with respect to their fully sodiated/desodiated counterparts. There are a few discrepancies between the DFT-predicted stabilities and experimental observations. NaMnMn(CN)<sub>6</sub> has been reported to be in the orthorhombic phase, whereas our DFT calculations show the rhombohedral phase to be the most stable.<sup>41</sup> NaCoFe(CN)<sub>6</sub> has been reported to be stable in the cubic phase, and two plateaus have been observed during charge/discharge processes.<sup>6</sup> In the DFT calculations, the cubic phase of NaCoFe(CN)<sub>6</sub> is nearly degenerate in energy



**Figure 2.** DFT-computed pseudo-binary stability diagrams of five known dry PBA compounds. All of the stable phases are in green color and unstable phases are in red. The filled markers denote the phases that have been observed experimentally.

Table 2. Spin State and Lattice Parameters of  $\text{Na}_2\text{MnFe}(\text{CN})_6 \cdot 2\text{H}_2\text{O}$ 

method	spin state	space group	lattice parameter
exp.	Mn: $t_{2g}^3 e_g^2$ , Fe: $t_{2g}^6$ (S)	$P2_1/c$	$a = 7.34, b = 7.53, c = 10.59$ $\alpha = 90, \beta = 92.1, \gamma = 90$
HSE	Mn: $t_{2g}^3 e_g^2$ , Fe: $t_{2g}^6$ (S)	$P1$	$a = 7.34, b = 7.46, c = 10.58$ $\alpha = 90, \beta = 92.6, \gamma = 90$

Figure 3. Optimized structure of  $\text{Na}_2\text{MnFe}(\text{CN})_6 \cdot 2\text{H}_2\text{O}$ .

with the monoclinic phase and lies only 1.4 meV/atom above the hull. We believe that these discrepancies are possibly due to the effect of water and vacancies in the PBA lattice. In particular, the insertion of Na ions can be largely hindered by  $\text{Fe}(\text{CN})_6$  vacancies, which has been reported to cause significant capacity fading.<sup>10</sup> Also, the fully desodiated  $\text{NiFe}(\text{CN})_6$  has not been reported experimentally to the authors' knowledge, and no phase transition has been observed when rhombohedral  $\text{Na}_2\text{NiFe}(\text{CN})_6$  is oxidized to  $\text{NaNiFe}(\text{CN})_6$  experimentally.<sup>46</sup> The DFT calculations find the tetragonal  $\text{NaNiFe}(\text{CN})_6$  to be the most stable phase, and the rhombohedral phase lies 3.8 meV/atom above the hull. We hypothesize that rhombohedral  $\text{NaNiFe}(\text{CN})_6$  is kinetically stabilized during fast charge/discharge processes.

### EFFECT OF WATER IN THE PBA LATTICE

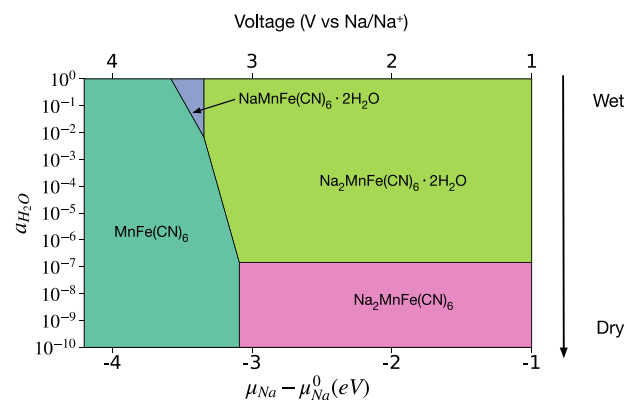
To probe the effect of water on PBAs, we have selected hydrated  $\text{Na}_2\text{MnFe}(\text{CN})_6 \cdot 2\text{H}_2\text{O}$  as a model system due to the availability of experimental data on  $\text{Na}_{1.89}\text{Mn}[\text{Fe}(\text{CN})_6]_{0.97} \cdot 1.87\text{H}_2\text{O}$ .<sup>3</sup> Initial structures were obtained by placing two  $\text{H}_2\text{O}$  molecules per formula unit at void spaces found by Voronoi tessellation in the cubic, tetragonal, monoclinic, and rhombohedral structures of dry  $\text{Na}_2\text{MnFe}(\text{CN})_6$ . The structures were then fully relaxed by HSE functional.

Table 2 shows the calculated ground spin state configurations and lattice parameters of the most stable hydrated structure, which are in good agreement with experimental observations.<sup>3</sup> However, the positions of Na ions and  $\text{H}_2\text{O}$  molecules in our relaxed  $\text{Na}_2\text{MnFe}(\text{CN})_6 \cdot 2\text{H}_2\text{O}$  structure are opposite to those reported by synchrotron XRD and neutron diffraction. As illustrated in Figure 3, the DFT calculations predict that Na ions occupy the interstitial sites and coordinate with four nearest N atoms, whereas  $\text{H}_2\text{O}$  molecules reside at the center of the void space. This configuration is predicted to be 6 eV per formula unit lower in energy than the experimentally reported structure. Similar results have been obtained by Xiao et al.<sup>18</sup> We also calculated other common hydrated PBAs, and similar Na– $\text{H}_2\text{O}$  arrangements were obtained. Given that XRD techniques are generally unable to distinguish lighter elements, we will use the lowest DFT energy-hydrated structure for subsequent analysis and

recommend that more advanced characterization, e.g., using neutron techniques, be carried out to confirm the positions of Na and O atoms in PBA structures. We also carried out similar calculations on  $\text{Fe}_4[\text{Fe}(\text{CN})_6]_3 \cdot 14\text{H}_2\text{O}$ , and our results showed good agreement with the experimental data (Table S4).

### Effect of Na and Water on the Structure of PBAs.

Figure 4 shows the grand potential phase diagram of

Figure 4. Grand potential phase diagram of  $\text{Na}_x\text{MnFe}(\text{CN})_6 \cdot n\text{H}_2\text{O}$ 

$\text{Na}_x\text{MnFe}(\text{CN})_6 \cdot n\text{H}_2\text{O}$ , where each colored region corresponds to a single stable phase. Qualitatively similar results were obtained for the other common PBAs and are shown in Figure S2. As the chemical potential of Na decreases, Na is extracted from the PBA structure (charging process). In extremely dry electrolytes ( $a_{\text{H}_2\text{O}} < 10^{-8}$ ), only the dry  $\text{Na}_x\text{MnFe}(\text{CN})_6$  structures are stable. As the activity of water increases, hydrated phases become stable over a wider range of Na chemical potentials/voltages, which in turn result in changes in the phase transition behavior upon Na intercalation and, hence, the voltage profile (see the next section).

It has been well established that nearly all low-defect, Na-rich PBAs contain water in the lattice when synthesized in aqueous environments. It is also known that the hydrated monoclinic  $\text{Na}_2\text{MnFe}(\text{CN})_6 \cdot n\text{H}_2\text{O}$  disappears after several charge/discharge cycles in organic electrolytes,<sup>3</sup> which is consistent with the lack of hydrated phases in the computed

grand potential diagram under extremely dry conditions. A reversible phase transition between the monoclinic hydrated  $\text{Na}_2\text{MnFe}(\text{CN})_6 \cdot x\text{H}_2\text{O}$  and rhombohedral dry  $\text{Na}_2\text{MnFe}(\text{CN})_6$  has also been observed upon drying in the vacuum followed by exposure to the humid air.<sup>3</sup>

Our calculations show that under the same conditions, the fully desodiated structures are much more water resistant compared with the sodiated ones. Although there have been reports of containing water molecules in Na-deficient PBAs, for example,  $\text{Fe}_4[\text{Fe}(\text{CN})_6]_3 \cdot 14\text{H}_2\text{O}$  and  $\text{K}_{0.04}\text{NiFe}(\text{CN})_6 \cdot 4\text{H}_2\text{O}$ ,<sup>2,40</sup> we believe that this is the effect of  $\text{Fe}(\text{CN})_6$  defects. Our calculations for the  $\text{Fe}_4[\text{Fe}(\text{CN})_6]_3$  structures containing different amounts of  $\text{H}_2\text{O}$  showed that in aqueous solutions, the hydrated  $\text{Fe}_4[\text{Fe}(\text{CN})_6]_3$  is more stable than their dry counterparts (Figure S5).

In dry electrolytes, a reversible phase transition between rhombohedral  $\text{Na}_2\text{MnFe}(\text{CN})_6$  and tetragonal  $\text{MnFe}(\text{CN})_6$  is predicted. During Na intercalation in wet electrolytes, different phase transition behaviors happen due to the co-intercalation of  $\text{H}_2\text{O}$  and Na ions. The crystal structure changes from monoclinic  $\text{Na}_2\text{MnFe}(\text{CN})_6 \cdot 2\text{H}_2\text{O}$  to tetragonal  $\text{MnFe}(\text{CN})_6$ .

Water molecules in the PBA lattice may also serve as “pillars” that facilitate low-strain charge/discharge processes.<sup>42,43</sup> Figure 5 shows the volume change of the three

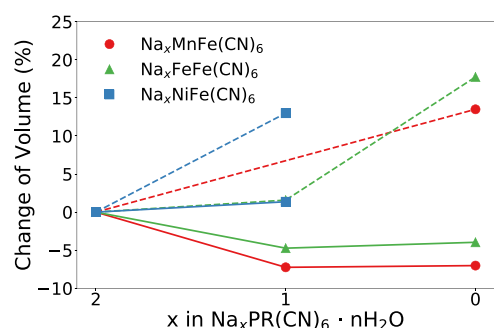


**Figure 5.** Volume change of PBAs upon Na deintercalation in wet (solid line) and dry (dashed line) electrolytes.

common PBA cathodes during charge processes with respect to their fully discharged states. It can be seen that in dry electrolytes, all cathodes undergo a volume expansion of 15–20% with the extraction of  $\text{Na}^+$ . In wet electrolytes, on the other hand,  $\text{Na}_2\text{FeMn}(\text{CN})_6$  and  $\text{Na}_2\text{FeFe}(\text{CN})_6$  undergo volume reductions of 7 and 4%, respectively, with the extraction of  $\text{Na}^+$ , whereas  $\text{Na}_2\text{NiFe}(\text{CN})_6$  undergoes only a small volume increase of 1.3%. The volume changes in wet electrolytes are, therefore, much smaller in magnitude compared to that in dry electrolytes, which may result in better cycling stabilities. These observations are in line with prior experimental results showing that  $\text{Na}_2\text{NiFe}(\text{CN})_6$  cathodes exhibit a near-zero capacity loss after 5000 cycles in aqueous electrolytes,<sup>8</sup> whereas capacity fading of 4% has been observed after only 200 cycles<sup>40</sup> in organic electrolytes. These results also point to the potential for naturally hydrated compounds to serve as electrode materials in alkali-ion batteries due to the distinct effect of the lattice water in electrochemical reactions. Several hydrated compounds have already been shown to exhibit great performance, such as  $\text{Na}_{0.71}\text{MnO}_2 \cdot n\text{H}_2\text{O}$ ,<sup>44</sup>  $\text{Zn}_{0.25}\text{V}_2\text{O}_5 \cdot n\text{H}_2\text{O}$ ,<sup>45</sup> and  $\text{FePO}_4 \cdot n\text{H}_2\text{O}$ .<sup>42</sup>

**Effect of Water on the Na Insertion Voltage.** Figure 6 shows the computed voltage profiles of the  $\text{Na}_x\text{MnFe}(\text{CN})_6$ ,  $\text{Na}_x\text{NiFe}(\text{CN})_6$ , and  $\text{Na}_x\text{FeFe}(\text{CN})_6$  PBAs in wet ( $a_{\text{H}_2\text{O}} = 1$ ), dry ( $a_{\text{H}_2\text{O}} = 10^{-4}$ ), and very-dry ( $a_{\text{H}_2\text{O}} = 10^{-9}$ ) electrolytes. The average voltage as a function of  $a_{\text{H}_2\text{O}}$  is plotted in Figure S3. In general, we observe that an increasing  $a_{\text{H}_2\text{O}}$  generally results in an increase in the voltage for all three PBAs. This is consistent with the increase of the redox potential of  $\text{Na}_2\text{MnFe}(\text{CN})_6$  in the aqueous electrolyte reported in the literature.<sup>46,47</sup>

For  $\text{Na}_x\text{MnFe}(\text{CN})_6$ , the DFT calculations predict only a single voltage plateau of 3.09 V for  $0 \leq x \leq 2$  in dry/very-dry electrolytes, whereas two voltage plateaus are predicted due to the emergence of the stable hydrated phase at intermediate Na concentrations in wet electrolytes. The single-plateau behavior in dry electrolytes is in line with the experimental findings of 3.44 V vs  $\text{Na}/\text{Na}^+$ .<sup>3</sup> Further, Pasta et al. have reported two plateaus at 3.5 and 4.0 V vs  $\text{Na}/\text{Na}^+$  for  $\text{Na}_{1.33}\text{Mn}[\text{Fe}$

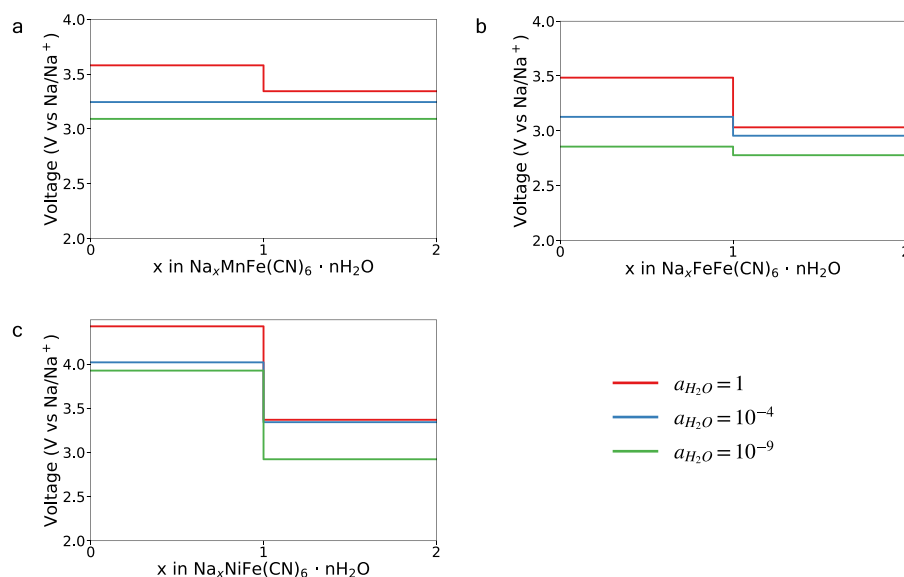


**Figure 6.** Na insertion voltage profiles of (a)  $\text{Na}_x\text{MnFe}(\text{CN})_6 \cdot n\text{H}_2\text{O}$ , (b)  $\text{Na}_x\text{NiFe}(\text{CN})_6 \cdot n\text{H}_2\text{O}$ , and (c)  $\text{Na}_x\text{FeFe}(\text{CN})_6 \cdot n\text{H}_2\text{O}$  for three water activities, representing wet ( $a_{\text{H}_2\text{O}} = 1$ ), dry ( $a_{\text{H}_2\text{O}} = 10^{-4}$ ), and very-dry ( $a_{\text{H}_2\text{O}} = 10^{-9}$ ) electrolytes.

(CN)<sub>6</sub>]<sub>0.79</sub> in a saturated NaClO<sub>4</sub> aqueous electrolyte, which is qualitatively consistent with our DFT predictions.<sup>46</sup> Similarly, it has been reported that Na<sub>2</sub>FeFe(CN)<sub>6</sub> exhibits two voltage plateaus at 3.0 and 3.29 V vs Na/Na<sup>+</sup> in a mixture of the DEC/EC electrolyte,<sup>5</sup> and the gap between the two plateaus becomes larger (3.1 and 4.0 V vs Na/Na<sup>+</sup>) in the 1 mol L<sup>-1</sup> Na<sub>2</sub>SO<sub>4</sub> aqueous electrolyte.<sup>5,48</sup> These observations are again in qualitative agreement with our calculations.

Our results predict that the voltage of Na<sub>2</sub>NiFe(CN)<sub>6</sub> in 0 ≤ x ≤ 1 varies from 3.92 to 4.43 V vs Na/Na<sup>+</sup>, which is beyond the stability window of aqueous solutions. Thus, only half of its theoretical capacity can be realized in the aqueous electrolyte. In fact, Ni<sup>2+</sup>/Ni<sup>3+</sup> is known to be electrochemically inactive in PBAs cathodes,<sup>8,40</sup> and this is confirmed by the integrated DFT spin densities, which show that in the active redox couple in Na<sub>2</sub>NiFe(CN)<sub>6</sub> is Fe<sup>2+→4+</sup> (see Figure S7a). The high voltage at 0 ≤ x ≤ 1 is due to the Fe<sup>3+→4+</sup> couple.

One further observation is that the HSE-predicted voltages, especially at high water activities, are generally underestimated relative to experiments.<sup>46,48</sup> One possible reason for this discrepancy may be the presence of defects, such as Fe(CN)<sub>6</sub> vacancies, which have been reported experimentally.<sup>3,49</sup> A further source of the discrepancy may be the choice of the value of the reference chemical potential of water, μ<sub>H<sub>2</sub>O(l)</sub><sup>0</sup>. The effect of the chemical potential of water on the phase stabilities of Na<sub>x</sub>MnFe(CN)<sub>6</sub>·nH<sub>2</sub>O system is shown in Figure 7a. From Figure 7a, we can see that when μ<sub>H<sub>2</sub>O(l)</sub> becomes less negative than μ<sub>H<sub>2</sub>O(l)</sub><sup>0</sup>, the fully hydrated NaMnFe(CN)<sub>6</sub>·nH<sub>2</sub>O is predicted to be stable across a wider range of Na concentrations. For μ<sub>H<sub>2</sub>O(l)</sub> > -18.96 eV, MnFe(CN)<sub>6</sub>·H<sub>2</sub>O becomes more stable than its dehydrated counterpart. The predicted Na insertion voltages as a function of μ<sub>H<sub>2</sub>O(l)</sub> are shown in Figure 7b. The predicted second voltage plateau (shown in Figure 7c) increases with μ<sub>H<sub>2</sub>O(l)</sub> and reaches a value of 3.90 V vs Na/Na<sup>+</sup> when MnFe(CN)<sub>6</sub>·H<sub>2</sub>O is stabilized relative to MnFe(CN)<sub>6</sub>, which is much closer to the experimentally observed voltage of 4.0 V vs Na/Na<sup>+</sup>.<sup>46</sup>

We also note that the predicted voltage of Na<sub>2</sub>NiFe(CN)<sub>6</sub> in dry electrolytes, which is 2.92 V vs Na/Na<sup>+</sup>, deviates from the experimental finding of 3.38 V vs Na/Na<sup>+</sup>.<sup>40</sup> This is mainly due to the different phase transition behaviors predicted by DFT calculations. In our calculations, a phase transition between rhombohedral Na<sub>2</sub>NiFe(CN)<sub>6</sub> and tetragonal NaNiFe(CN)<sub>6</sub> is predicted, whereas the rhombohedral Na<sub>2</sub>NiFe(CN)<sub>6</sub> is preserved in experiments possibly due to the metastability caused by fast charge/discharge processes.<sup>40</sup>

## SCREENING FOR PBA CATHODES FOR AQUEOUS NA-ION BATTERIES

Based on the above findings, we have performed a comprehensive screening for aqueous PBA cathodes. Only PBAs with R = Fe, Mn were considered given that they have been extensively studied experimentally, whereas P is allowed to be Ti, V, Cr, Mn, Fe, Co, Ni, Cu, Zn, Mo. Initial candidates for dry PR(CN)<sub>6</sub> and Na<sub>2</sub>PR(CN)<sub>6</sub> PBAs were first generated using the cubic/tetragonal and rhombohedral structures, respectively.

Figure 8 shows the HSE average voltages for the PBA candidates for two Na intercalation. It is observed that except P = Ti and Mo, the R = Mn PBAs generally exhibit lower average voltages than the R = Fe PBAs, which is due to the

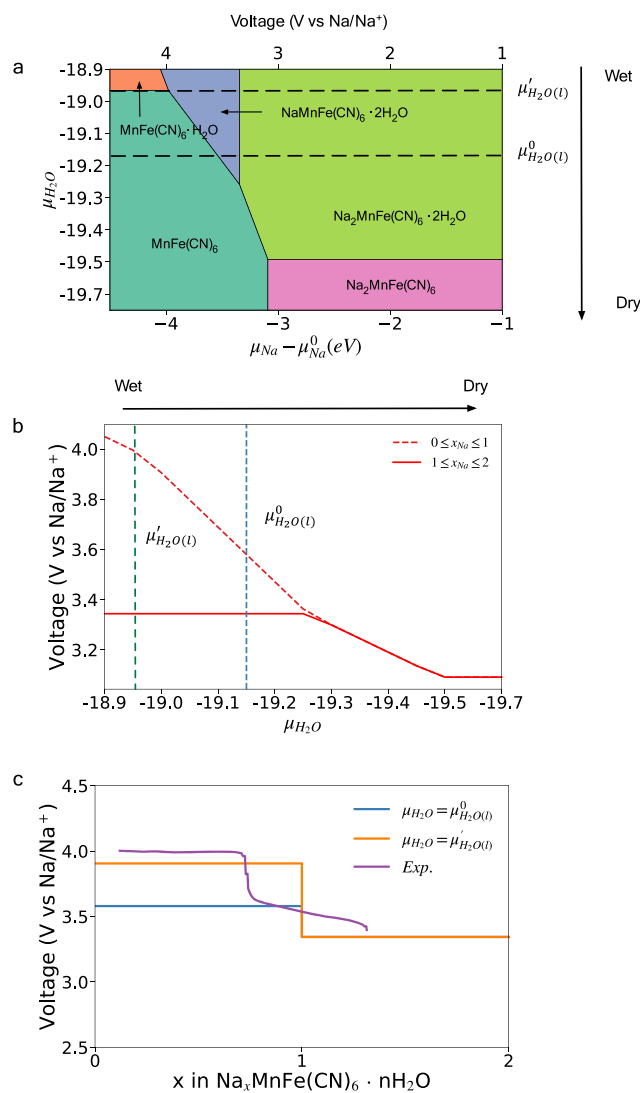


**Figure 7.** (a) Grand potential diagram of Na<sub>x</sub>MnFe(CN)<sub>6</sub>·nH<sub>2</sub>O. (b) Average Na insertion voltage for low (dashed line) and high (solid line) Na concentrations as a function of the electrolyte water content (μ<sub>H<sub>2</sub>O</sub>). (c) Voltage profile of Na<sub>x</sub>MnFe(CN)<sub>6</sub>·nH<sub>2</sub>O at μ<sub>H<sub>2</sub>O(l)</sub> = μ<sub>H<sub>2</sub>O(l)</sub><sup>0</sup>, μ<sub>H<sub>2</sub>O(l)</sub><sup>0</sup> and experimental results.<sup>46</sup>

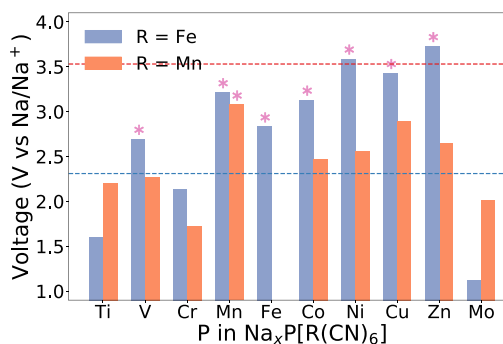


**Figure 8.** Predicted voltages for all initial candidates in the screening processes in the dry electrolyte. The cathodes that are known experimentally are marked with the asterisk. The red and blue lines are the potentials of O<sub>2</sub> and H<sub>2</sub> evolution in water, respectively.

lower standard potentials of Mn(CN)<sub>6</sub><sup>3-/4-</sup> compared to Fe(CN)<sub>6</sub><sup>3-/4-</sup>.<sup>50</sup> For P = Ti, the integrated DFT spin densities

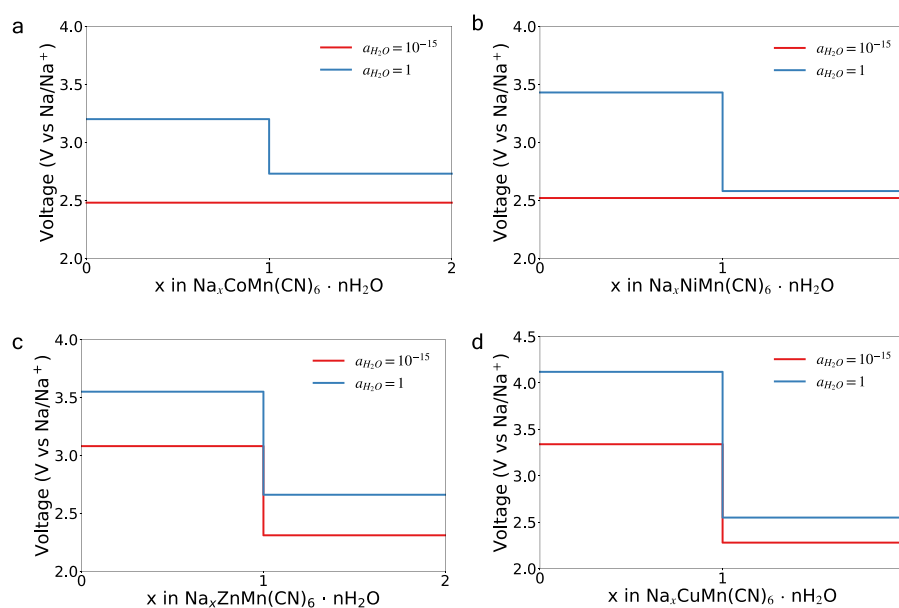


**Figure 9.** Predicted voltage profiles of the predicted PBAs cathodes.

(Figure S7g) show that the Ti undergoes a two-electron redox ( $2+ \rightarrow 4+$ ) instead of a one-electron ( $2+ \rightarrow 3+$ ) redox process on both the P and R sites. On the other hand, for the P = Ni, Cu, and Zn PBAs, the integrated DFT spin densities (see Figure S7a–f) show that the R cation, i.e., Mn or Fe, undergoes a two-electron redox from  $2+$  to  $4+$ . In the case of Ni, Mn/Fe oxidation to  $4+$  takes place preferentially to Ni oxidation. In the case of Cu and Zn, the  $3+$  oxidation state is generally not preferred. The voltages of the PBAs that have been investigated experimentally (denoted with asterisks) lie within/close to the  $\text{H}_2/\text{O}_2$  evolution limits.

Among the compositions that have not yet been studied experimentally,  $\text{Na}_2\text{CoMn}(\text{CN})_6$  is predicted to have a relatively high average voltage of 2.48 V. During Na deintercalation, both  $\text{Co}^{2+}$  and  $\text{Mn}^{2+}$  are electrochemically active and oxidized to  $\text{Co}^{3+}$  and  $\text{Mn}^{3+}$ .  $\text{Na}_2\text{NiMn}(\text{CN})_6$ ,  $\text{Na}_2\text{CuMn}(\text{CN})_6$ , and  $\text{Na}_2\text{ZnMn}(\text{CN})_6$  are also predicted to have relatively high average voltages of 2.52, 2.91, and 2.65 V, respectively, which is due to the two-electron redox of  $\text{Mn}^{2+ \rightarrow 4+}$ . It should be noted, however, that experimentally studied  $\text{Na}_2\text{CuFe}(\text{CN})_6$  and  $\text{Na}_2\text{ZnFe}(\text{CN})_6$  have been reported to exhibit only one-electron redox, likely due to the high voltage of the  $\text{Fe}^{3+ \rightarrow 4+}$  redox couple (DFT-predicted voltages of 3.81 and 4.24 V) beyond the  $\text{O}_2$  evolution limit. Further detailed investigations on the effects of hydration were performed on these candidates.

Figure 9 shows the DFT-computed voltage profiles for the four candidates in both wet and dry electrolytes. The corresponding computed pseudo-binary and grand potential phase diagrams are given in Figures S6 and S8, respectively. In dry electrolytes, both  $\text{Na}_x\text{CoMn}(\text{CN})_6$  and  $\text{Na}_x\text{NiMn}(\text{CN})_6$  are predicted to undergo a two-phase reaction upon charge from  $x = 2 \rightarrow 0$ , with a phase transition from rhombohedral to tetragonal and cubic phase, respectively. In wet electrolytes, an intermediate stable phase is observed at  $x = 1$ , which introduces a step in the voltage profile (blue lines in Figure 9a,b). The voltages of  $\text{Na}_2\text{CoMn}(\text{CN})_6$  and  $\text{Na}_2\text{NiMn}(\text{CN})_6$  are predicted to be 3.15/2.73 V and 3.43/2.58 V vs  $\text{Na}/\text{Na}^+$ , respectively.

In dry electrolytes, at  $x_{\text{Na}} = 1$ , monoclinic  $\text{NaZnMn}(\text{CN})_6$  and  $\text{NaCuMn}(\text{CN})_6$  are predicted to be stable and form two plateaus on their voltage profiles. The voltage of  $\text{Na}_x\text{ZnMn}(\text{CN})_6$  is predicted to be 3.08/2.31 V vs  $\text{Na}/\text{Na}^+$  in dry electrolytes and 3.55/2.66 V vs  $\text{Na}/\text{Na}^+$  in wet electrolytes.  $\text{Na}_x\text{CuMn}(\text{CN})_6$  has a voltage of 3.48/2.33 V vs  $\text{Na}/\text{Na}^+$  in dry electrolytes and the voltage increased to 4.12/2.55 V vs  $\text{Na}/\text{Na}^+$  in wet electrolytes.

## CONCLUSIONS

Using first-principles computations, we have performed a comprehensive analysis of the phase behavior of PBA cathodes for aqueous Na-ion batteries. A key contribution of our work is elucidating the effect of the lattice water on the phase stability and consequently the Na intercalation voltage profile. We have found that all dry PBA compounds undergo rhombohedral to cubic/tetragonal phase transitions during Na deintercalation. The presence of the lattice water raises the voltage and acts as pillars to reduce the volume change during electrochemical cycling, contributing to both higher energy density and better cycling stability. Using these insights, we have identified four new PBA compositions,  $\text{Na}_2\text{CoMn}(\text{CN})_6$ ,  $\text{Na}_2\text{NiMn}(\text{CN})_6$ ,  $\text{Na}_2\text{CuMn}(\text{CN})_6$ , and  $\text{Na}_2\text{ZnMn}(\text{CN})_6$ , that show great promise as aqueous Na-ion battery cathodes.

## ASSOCIATED CONTENT

### Supporting Information

The Supporting Information is available free of charge on the ACS Publications website at DOI: 10.1021/acs.chemmater.9b02269.

Spin-ordering effect on the phase stability of PBA compounds; comparison of different functionals in predicting properties of PBAs; calculated grand potential diagrams of  $\text{Na}_x\text{FeFe}(\text{CN})_6 \cdot x\text{H}_2\text{O}$  and  $\text{Na}_x\text{NiFe}(\text{CN})_6 \cdot x\text{H}_2\text{O}$  systems; computed voltage as a function of the activity of water; effect of  $\text{Fe}(\text{CN})_6$  defect; computed pseudo-binary phase diagrams of the predicted compounds; integrated spin density of the predicted

compounds; computed grand potential diagrams of the predicted compounds (PDF)

## AUTHOR INFORMATION

### Corresponding Author

\*E-mail: [ongsp@eng.ucsd.edu](mailto:ongsp@eng.ucsd.edu).

### ORCID

Xingyu Guo: 0000-0002-3456-5347

Zhenbin Wang: 0000-0002-7016-9245

Shyue Ping Ong: 0000-0001-5726-2587

### Notes

The authors declare no competing financial interest.

## ACKNOWLEDGMENTS

This work was supported by GEIRI North America under Project no. SGRIDGKJ[2017]841. The authors also acknowledge computing resources provided by Triton Shared Computing Cluster (TSCC) at UC San Diego, the National Energy Research Scientific Computing Center (NERSC), and the Extreme Science and Engineering Discovery Environment (XSEDE) supported by the National Science Foundation, under Grant no. ACI-1053575.

## REFERENCES

- (1) Kim, H.; Hong, J.; Park, K.-Y.; Kim, H.; Kim, S.-W.; Kang, K. Aqueous Rechargeable Li and Na Ion Batteries. *Chem. Rev.* **2014**, *114*, 11788–11827.
- (2) Herren, F.; Ludi, A.; Fischer, P.; Halg, W. Neutron Diffraction Study of Prussian Blue,  $\text{Fe}_4[\text{Fe}(\text{CN})_6]_3 \cdot \text{XH}_2\text{O}$ . Location of Water Molecules and Long-Range Magnetic Order. *Inorg. Chem.* **1980**, *19*, 956–959.
- (3) Song, J.; Wang, L.; Lu, Y.; Liu, J.; Guo, B.; Xiao, P.; Lee, J. J.; Yang, X. Q.; Henkelman, G.; Goodenough, J. B. Removal of Interstitial  $\text{H}_2\text{O}$  in Hexacyanometalates for a Superior Cathode of a Sodium-Ion Battery. *J. Am. Chem. Soc.* **2015**, *137*, 2658–2664.
- (4) Kareis, C. M.; Lapidus, S. H.; Her, J. H.; Stephens, P. W.; Miller, J. S. Non-Prussian Blue Structures and Magnetic Ordering of  $\text{Na}_2\text{Mn}^{\text{II}}[\text{Mn}^{\text{II}}(\text{CN})_6]$  and  $\text{Na}_2\text{Mn}^{\text{II}}[\text{Mn}^{\text{II}}(\text{CN})_6] \cdot 2\text{H}_2\text{O}$ . *J. Am. Chem. Soc.* **2012**, *134*, 2246–2254.
- (5) Wang, L.; Song, J.; Qiao, R.; Wray, L. A.; Hossain, M. A.; Chuang, Y.; de Yang, W.; Lu, Y.; Evans, D.; Lee, J. J.; et al. Rhombohedral Prussian White as Cathode for Rechargeable Sodium-Ion Batteries. *J. Am. Chem. Soc.* **2015**, *137*, 2548–2554.
- (6) Wu, X.; Wu, C.; Wei, C.; Hu, L.; Qian, J.; Cao, Y.; Ai, X.; Wang, J.; Yang, H. Highly Crystallized  $\text{Na}_2\text{CoFe}(\text{CN})_6$  with Suppressed Lattice Defects as Superior Cathode Material for Sodium-Ion Batteries. *ACS Appl. Mater. Interfaces* **2016**, *8*, 5393–5399.
- (7) Wu, X.; Deng, W.; Qian, J.; Cao, Y.; Ai, X.; Yang, H. Single-Crystal  $\text{FeFe}(\text{CN})_6$  Nanoparticles: A High Capacity and High Rate Cathode for Na-Ion Batteries. *J. Mater. Chem. A* **2013**, *1*, 10130–10134.
- (8) Wessells, C. D.; Peddada, S. V.; Huggins, R. A.; Cui, Y. Nickel Hexacyanoferrate Nanoparticle Electrodes for Aqueous Sodium and Potassium Ion Batteries. *Nano Lett.* **2011**, *11*, 5421–5425.
- (9) Lee, H. W.; Wang, R. Y.; Pasta, M.; Lee, S. W.; Liu, N.; Cui, Y. Manganese Hexacyanomanganate Open Framework as a High-Capacity Positive Electrode Material for Sodium-Ion Batteries. *Nat. Commun.* **2014**, *5*, No. 5280.
- (10) Qian, J.; Wu, C.; Cao, Y.; Ma, Z.; Huang, Y.; Ai, X.; Yang, H. Prussian Blue Cathode Materials for Sodium-Ion Batteries and Other Ion Batteries. *Adv. Energy Mater.* **2018**, *8*, No. 1702619.
- (11) Wessells, C. D.; Huggins, R. A.; Cui, Y. Copper Hexacyanoferrate Battery Electrodes with Long Cycle Life and High Power. *Nat. Commun.* **2011**, *2*, No. 550.
- (12) Ceder, G.; Aydinol, M. K.; Kohan, A. F. Application of First-Principles Calculations to the Design of Rechargeable Li-Batteries. *Comput. Mater. Sci.* **1997**, *8*, 161–169.
- (13) Kang, B.; Ceder, G. Battery Materials for Ultrafast Charging and Discharging. *Nature* **2009**, *458*, 190–193.
- (14) Ong, S. P.; Chevrier, V. L.; Hautier, G.; Jain, A.; Moore, C.; Kim, S.; Ma, X.; Ceder, G. Voltage, Stability and Diffusion Barrier Differences between Sodium-Ion and Lithium-Ion Intercalation Materials. *Energy Environ. Sci.* **2011**, *4*, 3680.
- (15) Lin, Y.-C.; Wen, B.; Wiaderek, K. M.; Sallis, S.; Liu, H.; Lapidus, S. H.; Borkiewicz, O. J.; Quackenbush, N. F.; Chernova, N. A.; Karki, K.; et al. Thermodynamics, Kinetics and Structural Evolution of  $\epsilon\text{-LiVOPO}_4$  over Multiple Lithium Intercalation. *Chem. Mater.* **2016**, *28*, 1794–1805.
- (16) Ceder, G.; Chiang, Y.-M.; Sadoway, D. R.; Aydinol, M. K.; Jang, Y.-L.; Huang, B. Identification of Cathode Materials for Lithium Batteries Guided by First-Principles Calculations. *Nature* **1998**, *392*, 694–696.
- (17) Ling, C.; Chen, J.; Mizuno, F. First-Principles Study of Alkali and Alkaline Earth Ion Intercalation in Iron Hexacyanoferrate: The Important Role of Ionic Radius. *J. Phys. Chem. C* **2013**, *117*, 21158–21165.
- (18) Xiao, P.; Song, J.; Wang, L.; Goodenough, J. B.; Henkelman, G. Theoretical Study of the Structural Evolution of a  $\text{Na}_2\text{FeMn}(\text{CN})_6$  Cathode upon Na Intercalation. *Chem. Mater.* **2015**, *27*, 3763–3768.
- (19) Kresse, G.; Furthmüller, J. Efficient Iterative Schemes for Ab Initio Total-Energy Calculations Using a Plane-Wave Basis Set. *Phys. Rev. B: Condens. Matter Mater. Phys.* **1996**, *54*, 11169–11186.
- (20) Blöchl, P. E. Projector Augmented-Wave Method. *Phys. Rev. B: Condens. Matter Mater. Phys.* **1994**, *50*, 17953–17979.
- (21) Heyd, J.; Scuseria, G. E.; Ernzerhof, M. Hybrid Functionals Based on a Screened Coulomb Potential. *J. Chem. Phys.* **2003**, *118*, 8207–8215.
- (22) Perdew, J. P.; Burke, K.; Ernzerhof, M. Generalized Gradient Approximation Made Simple. *Phys. Rev. Lett.* **1996**, *77*, 3865–3868.
- (23) Kulik, H. J.; Cococcioni, M.; Scherlis, D. A.; Marzari, N. Density Functional Theory in Transition-Metal Chemistry: A Self-Consistent Hubbard U Approach. *Phys. Rev. Lett.* **2006**, *97*, No. 103001.
- (24) Peng, H.; Yang, Z.-H.; Perdew, J. P.; Sun, J. Versatile van Der Waals Density Functional Based on a Meta-Generalized Gradient Approximation. *Phys. Rev. X* **2016**, *6*, No. 041005.
- (25) Shimamoto, N.; Ohkoshi, S.; Sato, O.; Hashimoto, K. Control of Charge-Transfer-Induced Spin Transition Temperature on Cobalt–Iron Prussian Blue Analogues. *Inorg. Chem.* **2002**, *41*, 678–684.
- (26) Fornasieri, G.; Bordage, A.; Bleuzen, A. Magnetism and Photomagnetism of Prussian Blue Analogue Nanoparticles Embedded in Porous Metal Oxide Ordered Nanostructures: Magnetism and Photomagnetism of Prussian Blue Analogue Nanoparticles Embedded in Porous Metal Oxide Ordered Nanostructures. *Eur. J. Inorg. Chem.* **2018**, *2018*, 259–271.
- (27) Nishino, M.; Kubo, S.; Yoshioka, Y.; Nakamura, A.; Yamaguchi, K. Theoretical Studies on Magnetic Interactions in Prussian Blue Analogs and Active Controls of Spin States by External Fields. *Mol. Cryst. Liq. Cryst. Sci. Technol., Sect. A* **1997**, *305*, 109–128.
- (28) Ong, S. P.; Richards, W. D.; Jain, A.; Hautier, G.; Kocher, M.; Cholia, S.; Gunter, D.; Chevrier, V. L.; Persson, K. A.; Ceder, G. Python Materials Genomics (Pymatgen): A Robust, Open-Source Python Library for Materials Analysis. *Comput. Mater. Sci.* **2013**, *68*, 314–319.
- (29) Aydinol, M. K.; Kohan, A. F.; Ceder, G.; Cho, K.; Joannopoulos, J. Ab Initio Study of Lithium Intercalation in Metal Oxides and Metal Dichalcogenides. *Phys. Rev. B* **1997**, *56*, 1354–1365.
- (30) Ong, S. P.; Wang, L.; Kang, B.; Ceder, G. Li–Fe–P–O<sub>2</sub> Phase Diagram from First Principles Calculations. *Chem. Mater.* **2008**, *20*, 1798–1807.

- (31) Sai Gautam, G. S.; Canepa, P.; Richards, W. D.; Malik, R.; Ceder, G. Role of Structural H<sub>2</sub>O in Intercalation Electrodes: The Case of Mg in Nanocrystalline Xerogel-V<sub>2</sub>O<sub>5</sub>. *Nano Lett.* **2016**, *16*, 2426–2431.
- (32) Nørskov, J. K.; Rossmeisl, J.; Logadottir, A.; Lindqvist, L.; Kitchin, J. R.; Bligaard, T.; Jónsson, H. Origin of the Overpotential for Oxygen Reduction at a Fuel-Cell Cathode. *J. Phys. Chem. B* **2004**, *108*, 17886–17892.
- (33) Linstrom, P. J., Eds. Mallard, W. G. *NIST Chemistry WebBook, NIST Standard Reference Database Number 69*; National Institute of Standards and Technology: Gaithersburg, MD, 20899.
- (34) Bergerhoff, G.; Hundt, R.; Sievers, R.; Brown, I. D. The Inorganic Crystal Structure Data Base. *J. Chem. Inf. Model.* **1983**, *23*, 66–69.
- (35) Wojdeł, J. C.; Moreira, I. de P. R.; Bromley, S. T.; Illas, F. On the Prediction of the Crystal and Electronic Structure of Mixed-Valence Materials by Periodic Density Functional Calculations: The Case of Prussian Blue. *J. Chem. Phys.* **2008**, *128*, No. 044713.
- (36) Jain, A.; Ong, S. P.; Hautier, G.; Chen, W.; Richards, W. D.; Dacek, S.; Cholia, S.; Gunter, D.; Skinner, D.; Ceder, G.; et al. Commentary: The Materials Project: A Materials Genome Approach to Accelerating Materials Innovation. *APL Mater.* **2013**, *1*, No. 011002.
- (37) Wang, L.; Maxisch, T.; Ceder, G. Oxidation Energies of Transition Metal Oxides within the GGA + U Framework. *Phys. Rev. B* **2006**, *73*, No. 195107.
- (38) Perdew, J. P.; Ruzsinszky, A.; Csonka, G. I.; Vydrov, O. A.; Scuseria, G. E.; Constantin, L. A.; Zhou, X.; Burke, K. Restoring the Density-Gradient Expansion for Exchange in Solids and Surfaces. *Phys. Rev. Lett.* **2008**, *100*, No. 136406.
- (39) Sun, J.; Ruzsinszky, A.; Perdew, J. P. Strongly Constrained and Appropriately Normed Semilocal Density Functional. *Phys. Rev. Lett.* **2015**, *115*, No. 036402.
- (40) Ji, Z.; Han, B.; Liang, H.; Zhou, C.; Gao, Q.; Xia, K.; Wu, J. On the Mechanism of the Improved Operation Voltage of Rhombohedral Nickel Hexacyanoferrate as Cathodes for Sodium-Ion Batteries. *ACS Appl. Mater. Interfaces* **2016**, *8*, 33619–33625.
- (41) Lee, H. W.; Wang, R. Y.; Pasta, M.; Lee, S. W.; Liu, N.; Cui, Y. Manganese Hexacyanomanganate Open Framework as a High-Capacity Positive Electrode Material for Sodium-Ion Batteries. *Nat. Commun.* **2014**, *5*, No. 5280.
- (42) Lim, S. Y.; Lee, J. H.; Kim, S.; Shin, J.; Choi, W.; Chung, K. Y.; Jung, D. S.; Choi, J. W. Lattice Water for the Enhanced Performance of Amorphous Iron Phosphate in Sodium-Ion Batteries. *ACS Energy Lett.* **2017**, *2*, 998–1004.
- (43) Li, C.; Gu, L.; Tong, J.; Tsukimoto, S.; Maier, J. A Mesoporous Iron-Based Fluoride Cathode of Tunnel Structure for Rechargeable Lithium Batteries. *Adv. Funct. Mater.* **2011**, *21*, 1391–1397.
- (44) Nam, K. W.; Kim, S.; Yang, E.; Jung, Y.; Levi, E.; Aurbach, D.; Choi, J. W. Critical Role of Crystal Water for a Layered Cathode Material in Sodium Ion Batteries. *Chem. Mater.* **2015**, *27*, 3721–3725.
- (45) Kundu, D.; Adams, B. D.; Duffort, V.; Vajargah, S. H.; Nazar, L. F. A High-Capacity and Long-Life Aqueous Rechargeable Zinc Battery Using a Metal Oxide Intercalation Cathode. *Nat Energy* **2016**, *1*, No. 16119.
- (46) Pasta, M.; Wang, R. Y.; Ruffo, R.; Qiao, R.; Lee, H. W.; Shyam, B.; Guo, M.; Wang, Y.; Wray, L. A.; Yang, W.; et al. Manganese-Cobalt Hexacyanoferrate Cathodes for Sodium-Ion Batteries. *J. Mater. Chem. A* **2016**, *4*, 4211–4223.
- (47) Nakamoto, K.; Sakamoto, R.; Ito, M.; Kitajou, A.; Okada, S. Effect of Concentrated Electrolyte on Aqueous Sodium-Ion Battery with Sodium Manganese Hexacyanoferrate Cathode. *Electrochemistry* **2017**, *85*, 179–185.
- (48) Wu, X.; Luo, Y.; Sun, M.; Qian, J.; Cao, Y.; Ai, X.; Yang, H. Low-Defect Prussian Blue Nanocubes as High Capacity and Long Life Cathodes for Aqueous Na-Ion Batteries. *Nano Energy* **2015**, *13*, 117–123.
- (49) You, Y.; Wu, X.-L.; Yin, Y.-X.; Guo, Y.-G. High-Quality Prussian Blue Crystals as Superior Cathode Materials for Room-Temperature Sodium-Ion Batteries. *Energy Environ. Sci.* **2014**, *7*, 1643–1647.
- (50) Stanislav, K.; Ladislav, S. *Handbook of Chemical Equilibria in Analytical Chemistry*; Ellis Horwood Ltd.: Chichester, 1985.